shore birds (*22*), and interdigital webbing has been reported in theropod dinosaurs (*29*).

Reduction of the pelvic girdle and hindlimb and the concomitant enhancement of axial-powered locomotion are common among semiaquatic vertebrates. The flexibility of the tail and the form of the neural spines in *Spinosaurus* suggest tail-assisted swimming. Like extinct and extant semiaquatic reptiles, *Spinosaurus* used lateral undulation of the tail, in contrast to the vertical axial undulation adopted repeatedly by semi-aquatic mammals (*20*, *21*).

The dorsal "sail" in *Spinosaurus*, the tallest axial structure documented among dinosaurs, has been argued to be a thermoregulatory surface, a muscle- or fat-lined hump (*30*), or a display structure. Stromer (*1*) drew an analogy to the skin-covered neural spines of the crested chameleon, *Trioceros cristatus* (Fig. 4E). As in *T. cristatus*, the sail of *Spinosaurus* is centered over the trunk (Fig. 2A). The shape and positioning of the spine are also similar, and the base of the neural spine is expanded anteroposteriorly, with edges marked by ligament scars (Fig. 2E). In *Trioceros*, a tendon of multisegmental axial musculature attaches to the expanded base of the neural spine (Fig. 4E). The upper portion of the spine has sharp anterior and posterior edges, is marked by fine vertical striae (Figs. 2E and 4D), and is spaced away from adjacent spines, unlike the broader, contiguous, paddle-shaped dorsal spines of other spinosaurids (*13*). The striated surface, sharp edges, and dense, poorly vascularized internal bone of the spines suggest that they were wrapped snugly in skin and functioned as a display structure that would have remained visible while swimming.

REFERENCES AND NOTES

1. E. Stromer, *Ahb. Königl. Bayer. Akad. Wissen. Math-Phys. Kl.* **28**, 1–32 (1915).
2. E. Stromer, *Abh. Königl. Bayer. Akad. Wissen. Math.-Naturwissen. Abt.* **22**, 1–79 (1934).
3. J. B. Smith, M. C. Lamanna, H. Mayr, K. J. Lacovara, *J. Paleontol.* **80**, 400–406 (2006).
4. W. Nothdurft, J. Smith, *The Lost Dinosaurs of Egypt* (Random House, New York, 2002).
5. P. Taquet, D. Russell, *C. R. Acad. Sci. Paris* **299**, 347–353 (1998).
6. C. Dal Sasso, S. Maganuco, E. Buffetaut, M. A. Mendez, *J. Vert. Paleontol.* **25**, 888–896 (2005).
7. P. C. Sereno *et al.*, *Science* **272**, 986–991 (1996).
8. See the supplementary materials on *Science* Online.
9. R. Lavocat, in *Comptes Rendus de la 19ème Congrès Géologique International*, Alger, 1952, session XII-3, 15 (1954), pp. 65–68.
10. L. Mahler, *J. Vert. Paleont.* **25**, 236–239 (2005).
11. D. A. Russell, *Bull. Mus. Hist. Nat. Paris* **18**, 349–402 (1996).
12. B. McFeeters, M. J. Ryan, S. Hinic-Frlog, C. Schröder-Adams, H. Sues, *Can. J. Earth Sci.* **50**, 636–649 (2013).
13. P. C. Sereno *et al.*, *Science* **282**, 1298–1302 (1998).
14. A. J. Charig, A. C. Milner, *Bull. Nat. Hist. Mus* **53**, 11–70 (1997).
15. C. Brochu, *J. Vert. Paleontol. Mem. 7*, **22** (suppl. 4), 1–138 (2002).
16. D. B. Leitch, K. C. Catania, *J. Exp. Biol.* **215**, 4217–4230 (2012).
17. F. E. Novas, F. Dalla Vecchia, D. F. Pais, *Rev. Mus. Argent. Cien. Nat.* **7**, 167–175 (2005).
18. F. E. Fish, G. V. Lauder, *Annu. Rev. Fluid Mech.* **38**, 193–224 (2006).
19. S. I. Madar, *Adv. Vert. Paleobiol.* **1**, 353–378 (1998).
20. P. D. Gingerich, *Paleobiology* **29**, 429–454 (2003).
21. F. E. Fish, *IEEE J. Oceanic Eng.* **29**, 605–621 (2004).
22. A. Manegold, *Acta Ornithol.* **41**, 79–82 (2006).
23. E. Amson, C. de Muizon, M. Laurin, C. Argot, V. de Buffrénil, *Proc. Biol. Sci.* **281**, 20140192 (2014).
24. K. T. Bates, R. B. J. Benson, P. L. Falkingham, *Paleobiology* **38**, 486–507 (2012).
25. S. M. Gatesy, M. Bäker, J. R. Hutchinson, *Paleobiology* **29**, 535–544 (2009).
26. E. Stromer, *Abh. Königl. Bayer. Akad. Wissen. Math.-Naturwissen. Abt.* **33**, 1–102 (1936).
27. A. J. Charig, A. C. Milner, *Nature* **324**, 359–361 (1986).
28. E. J. Rayfield, A. C. Milner, V. B. Xuan, P. G. Young, *J. Vert. Paleontol.* **27**, 892–901 (2007).
29. M. L. Casanovas Cladellas *et al.*, *España Zub. Monogr.* **5**, 135–163 (1993).
30. J. B. Bailey, *J. Paleontol.* **71**, 1124–1146 (1997).

NEUROSCIENCE

A critical time window for dopamine actions on the structural plasticity of dendritic spines

Sho Yagishita,[1,2] Akiko Hayashi-Takagi,[1,2,3] Graham C.R. Ellis-Davies,[4] Hidetoshi Urakubo,[5] Shin Ishii,[5] Haruo Kasai[1,2]*

Animal behaviors are reinforced by subsequent rewards following within a narrow time window. Such reward signals are primarily coded by dopamine, which modulates the synaptic connections of medium spiny neurons in the striatum. The mechanisms of the narrow timing detection, however, remain unknown. Here, we optically stimulated dopaminergic and glutamatergic inputs separately and found that dopamine promoted spine enlargement only during a narrow time window (0.3 to 2 seconds) after the glutamatergic inputs. The temporal contingency was detected by rapid regulation of adenosine 3′,5′-cyclic monophosphate in thin distal dendrites, in which protein-kinase A was activated only within the time window because of a high phosphodiesterase activity. Thus, we describe a molecular basis of reinforcement plasticity at the level of single dendritic spines.

Animal behaviors are reinforced only when rewarded shortly after a motor or sensory event (*1*, *2*). The neocortex, hippocampus, and amygdala process the sensorimotor signals and send glutamatergic synaptic output to the striatum (*3*), where connections can be modified by Hebbian learning mechanisms, such as spike-timing-dependent plasticity (STDP) (*4*). Animals learn to associate the sensorimotor signals with subsequent rewards through reinforcement of the neuronal circuits involving dopamine (*5–7*). Despite its importance, this narrow timing detection has never been demonstrated at the cellular level and might be ascribed to neural network properties (*6*, *8*).

Dendritic spine morphology is correlated with spine function (*9*), and dendritic spines enlarge during long-term potentiation in the cortices (*10–12*). We examined the effects of dopamine on the structural plasticity in striatal medium spiny neurons (MSNs). Results show that dopamine affected spine structural plasticity in a narrow time window consistent with behavioral conditioning (*5*). Functional imaging revealed the molecular interrelationships between the reinforcement and Hebbian plasticity.

We investigated dopamine actions on glutamatergic synapses on MSNs using optogenetics and

[1]Laboratory of Structural Physiology, Center for Disease Biology and Integrative Medicine, Faculty of Medicine, The University of Tokyo, Bunkyo-ku, Tokyo 113-0033, Japan. [2]Core Research for Evolutional Science and Technology, Japan Science and Technology Agency, Japan Science and Technology Agency, 4-1-8 Honcho, Kawaguchi, Saitama 332-0012, Japan. [3]Precursory Research for Embryonic Science and Technology, Japan Science and Technology Agency, Japan Science and Technology Agency, 4-1-8 Honcho, Kawaguchi, Saitama 332-0012, Japan. [4]Department of Neuroscience, Mount Sinai School of Medicine, New York, NY 10029, USA. [5]Integrated Systems Biology Laboratory, Department of Systems Science, Graduate School of Informatics, Kyoto University, Sakyo-ku, Kyoto 606-8501, Japan.
*Corresponding author. E-mail: hkasai@m.u-tokyo.ac.jp

two-photon uncaging. For optogenetic stimulation of dopaminergic fibers, a Cre-dependent adeno-associated virus (AAV) vector expressing channelrhodopsin-2 (ChR2) was injected into the ventral tegmental area (VTA) of DAT-Cre mice

expressing Cre specific to dopaminergic neurons (Fig. 1A and fig. S1). The direct pathway–constituting MSNs, which mainly express dopamine 1 receptors (D1Rs) (13), were labeled by an AAV vector with a specific promoter for D1R-MSNs (Fig. 1A

and fig. S1). In acute coronal slices, including the nucleus accumbens (NAc) core, whole-cell recordings were obtained from the identified D1R-MSNs. Dendritic spines were visualized by means of two-photon microscopy (980 nm) detecting
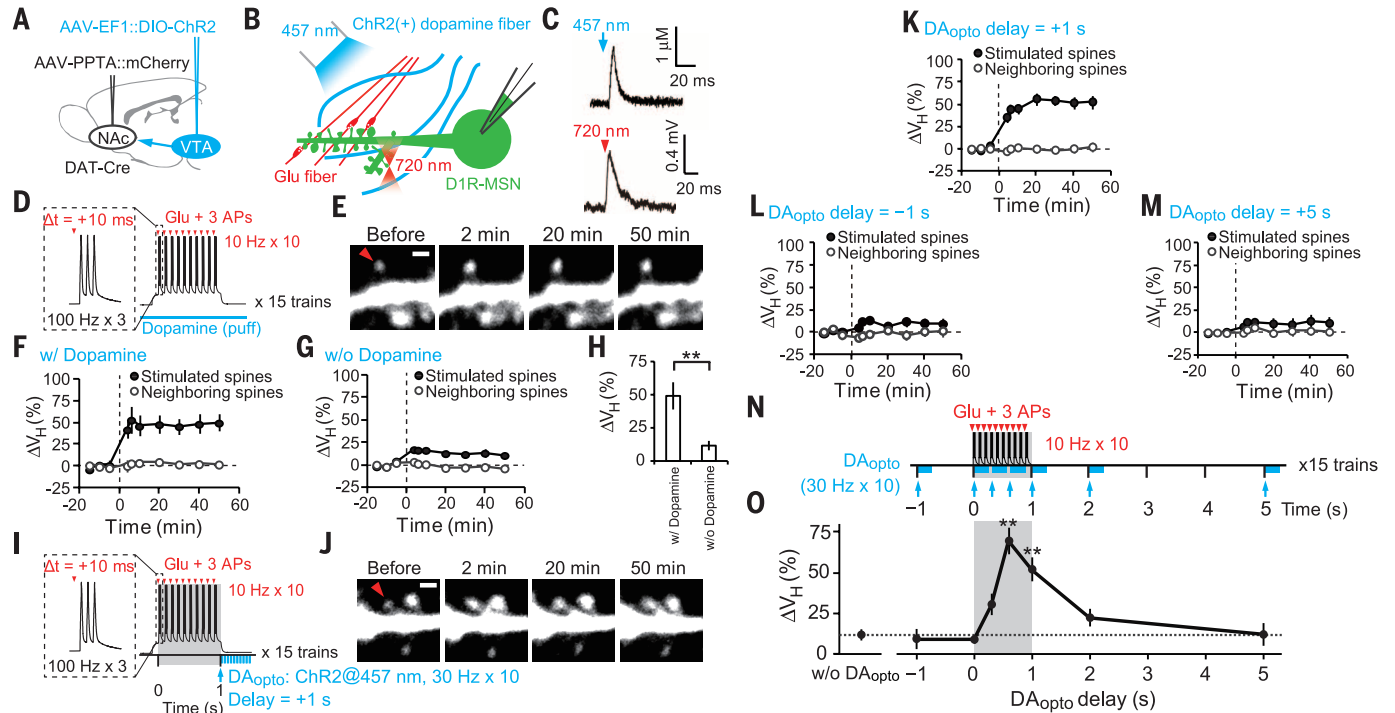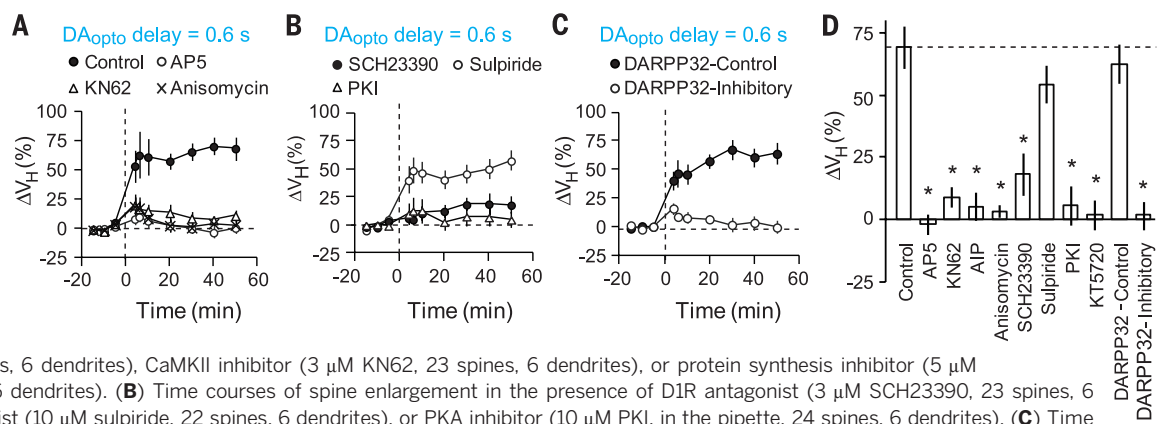

Fig. 1. A temporal profile of dopamine actions on spine enlargement. (**A**) Injection of AAV vectors for ChR2 and the D1R-MSN marker (PPTA-mCherry) in 3-week-old DAT-Cre mice. (**B**) Selective stimulation of dopaminergic and glutamatergic inputs by means of blue laser field irradiation to ChR2 and two-photon uncaging of caged-glutamate at a single spine, respectively, in acute slices of NAc obtained from 5- to 7-week-old mice. (**C**) An amperometric measurement of dopamine (top) by carbon-fiber electrode and whole-cell recording of glutamate-induced current (bottom, 2pEPSP) in identified D1R-MSNs. (**D**) An STDP protocol with dopamine puff application. (**E**) Images of the dendritic spine (red arrowhead) that received STDP stimulation in the presence of dopamine (100 μM). (**F** and **G**) Time courses of spine enlargement in the presence [(F), 13 spines, 4 dendrites] and absence of

dopamine [(G), 58 spines, 14 dendrites]. (**H**) Amplitudes of spine enlargements with or without dopamine. **$P = 0.0041$ by Mann-Whitney U test. (**I**) STDP with repetitive activation of dopaminergic fibers containing ChR2 (blue lines) at 30 Hz, 10 times (DA$_{opto}$). (**J**) Images of the dendritic spine (arrowhead) that received STDP + DA$_{opto}$ with a delay of 1 s. (**K** to **M**) Time courses of spine enlargement induced by STDP + DA$_{opto}$ at 1 s [(K), 48 spines, 14 dendrites], −1 s [(L), 20 spines, 5 dendrites] and 5 s [(M), 28 spines, 7 dendrites] after STDP onset. (**N**) Timings of DA$_{opto}$ application. (**O**) Increases in spine volumes by STDP + DA$_{opto}$ plotted versus DA$_{opto}$ delay (fig. S2, A to C). Data are presented as mean ± SEM. $P = 4.2 \times 10^{-6}$ with Kruskal-Wallis and **$P = 0.0018$ (0.6 s) and 0.0027 (1 s) by Steel test in comparison with STDP in the absence of DA$_{opto}$. Scale bars, 1 μm.

Fig. 2. Pharmacology of spine enlargement induced by STDP plus DA$_{opto}$ with a 0.6-s delay. (**A**) Time courses of spine enlargement induced by STDP + DA$_{opto}$ with a 0.6-s delay in the absence (control, 24 spines, 7 dendrites) and presence of NMDAR antagonist (50 μM D-AP5, 22 spines, 6 dendrites), CaMKII inhibitor (3 μM KN62, 23 spines, 6 dendrites), or protein synthesis inhibitor (5 μM anisomycin, 25 spines, 6 dendrites). (**B**) Time courses of spine enlargement in the presence of D1R antagonist (3 μM SCH23390, 23 spines, 6 dendrites), D2R antagonist (10 μM sulpiride, 22 spines, 6 dendrites), or PKA inhibitor (10 μM PKI, in the pipette, 24 spines, 6 dendrites). (**C**) Time courses of spine enlargement in the presence of inhibitory (100 μM, in the pipette, 24 spines, 6 dendrites) or control peptide for DARPP-32 (100 μM, in the pipette, 24 spines, 6 dendrites). (**D**) Averaged volume changes in the absence and presence of the compounds. Data are presented as mean ± SEM. $P = 3.4 \times 10^{-6}$ with Kruskal-Wallis and *$P = 0.023$ (AP5), 0.023 (KN62), 0.037 (AIP) (fig. S5A), 0.023 (anisomycin), 0.035 (SCH23390), 0.023 (PKI), 0.037 (KT5720) (fig. S5A), and 0.023 (DARPP-32 inhibitory peptide) with Steel test.

fluorescence of Alexa488 loaded through a recording pipette (Fig. 1B and fig. S1C). Stimulation of a single spine by means of two-photon uncaging (720 nm) of CDNI-Glu (Fig. 1B) induced two-photon excitatory postsynaptic potentials (2pEPSPs) with amplitudes similar to miniature EPSPs (mEPSPs) (Fig. 1C and fig. S1D). The amplitudes of 2pEPSCs positively correlated with spine volumes, as they did with pyramidal neurons (fig. S1E) (9). The STDP protocol of repetitive uncaging of glutamate paired with action potentials (APs) (Glu + AP) (Fig. 1D) (14) induced robust spine enlargement that was selective for the stimulated spine (Fig. 1, E and F) when dopamine (100 µM) was puff applied, whereas only a weak enlargement occurred in the absence of dopamine (Fig. 1G), which is consistent with previous findings (14, 15).

A single pulse of blue laser stimulation of ChR2-expressing dopaminergic fibers induced a transient increase in the tissue dopamine concentration (Fig. 1C). We tested the actions of a physiologically relevant phasic release of dopamine (30 Hz, 10 times) induced by the optogenetic stimulation of dopaminergic fibers (DA_{opto}) and found that DA_{opto} just after STDP stimulation (DA_{opto} delay = 1 s) (Fig. 1I) induced

Fig. 3. DA_{opto} effects on STDP stimulation-induced increases in $[Ca^{2+}]_i$ and CaMKII activities. (**A** and **B**) Increases in Fluo4-FF fluorescence, representing $[Ca^{2+}]_i$ increases, within single spines in response to a train of STDP stimulation in the absence [(A), 20 spines, 15 dendrites] and presence of DA_{opto} with a 0.6-s delay [(B), 15 spines, 8 dendrites]. Blue laser irradiation during DA_{opto} is blanked by the blue bar. (**C**) STDP and DA_{opto} protocols for Ca^{2+} and CaMKII imaging. Unlike plasticity induction (Fig. 1N), only one train was applied. (**D**) No effect of DA_{opto} on the peak values of $[Ca^{2+}]_i$ (fig. S6, A to C). $P = 0.91$ with Kruskal-Wallis test. (**E** and **F**) Ratiometric imaging with Camuiα-CR during STDP stimulation in the absence [(E), 33 spines, 14 dendrites] or presence of DA_{opto} with a 0.6-s delay [(F), 42 spines, 14 dendrites]. Relative increases in the ratio are shown as pseudocolor coding in (E). (Bottom) Time courses of FRET ratios in the spines stimulated with glutamate uncaging or the neighboring spines. Scale bars, 1 µm. (**G**) Dependence of the peak Camuiα-CR FRET ratios on the DA_{opto} delay (fig. S6, D to F). $P = 1.3 \times 10^{-5}$ with Kruskal-Wallis test and ***$P = 8.4 \times 10^{-5}$ with Steel test versus those without DA_{opto}. (**H**) Normalized increases in Camuiα-CR ratios by STDP + DA_{opto} with a 0.6-s delay in the stimulated (42 spines, 14 dendrites) and neighboring spines (42 spines, 14 dendrites), and in the presence of DARPP-32 inhibitory peptide in the stimulated spines (43 spines, 10 dendrites) (fig. S6G). Data are presented as mean ± SEM. $P = 8.8 \times 10^{-9}$ with Kruskal-Wallis test and *** $P = 2.6 \times 10^{-9}$ and 1.1×10^{-6} with Steel test.
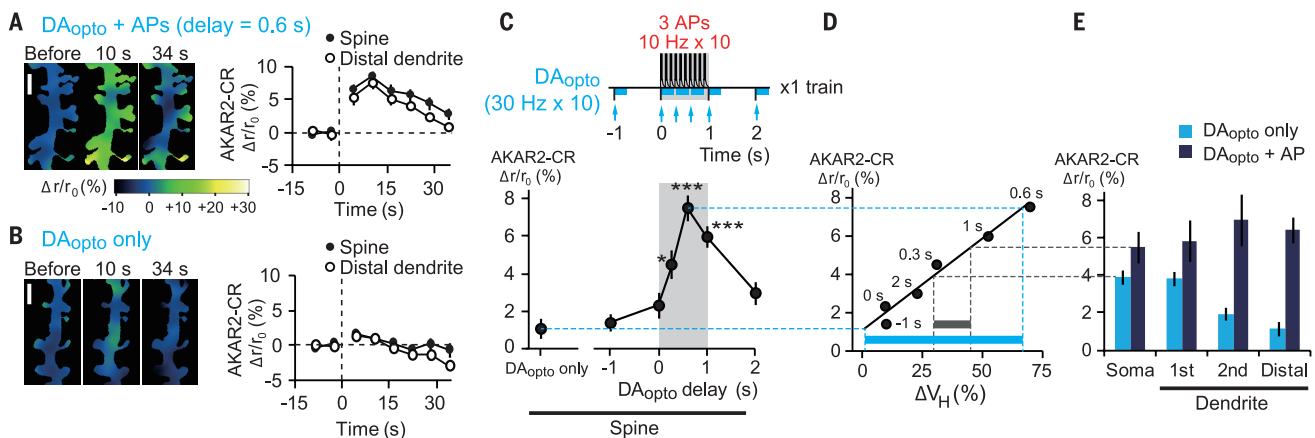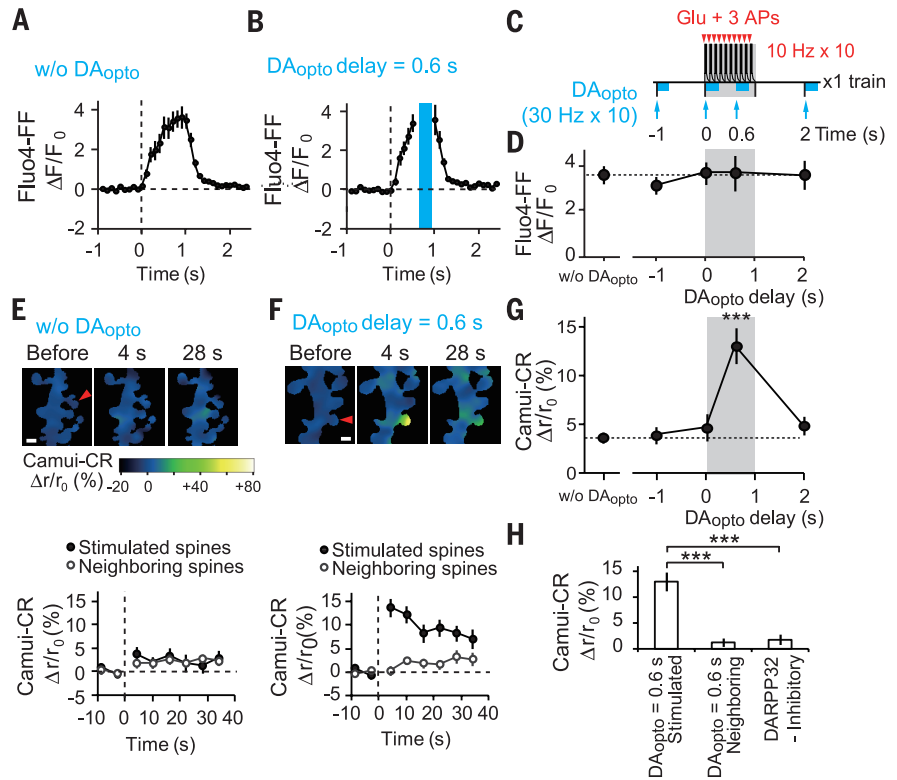

Fig. 4. AP effects on DA_{opto}-induced PKA activation in proximal and distal dendrites. (**A** and **B**) Images and time courses of FRET ratios of AKAR2-CR in the spine and distal dendrites stimulated by APs + DA_{opto} with a 0.6-s delay [(A), 153 spines, 25 dendrites] or DA_{opto} only [(B), 158 spines, 26 dendrites]. The relative increases in the ratio were pseudocolor coded as shown in (A). Scale bar, 2 µm. (**C**) AKAR2-CR responses to APs + DA_{opto} with various delays (fig. S7, E to I). $P = 5.3 \times 10^{-10}$ with Kruskal-Wallis test and *$P = 0.012$, ***$P = 1.3 \times 10^{-6}$ (0.6 s), and 4.0×10^{-4} (1 s) with Steel test versus DA_{opto} only. (**D**) AKAR2-CR response (C) plotted against spine volume changes (Fig. 1O) for various DA_{opto} timings. The Spearman's correlation coefficient was 0.94, and $P = 0.0048$. The blue and gray bars indicate the dynamic ranges of volume changes predicted by the dynamic ranges of AKAR2 responses at dendritic spine (blue) and soma (gray). (**E**) AKAR2-CR responses at the soma and first, second, and distal dendrites in response to DA_{opto} only and DA_{opto} + APs with a 0.6-s delay (fig. S8, A and B).

robust spine enlargement (Fig. 1, J and K). Stimulation of dopaminergic fibers 1 s before (DA_{opto} delay = −1 s) or 5 s after (DA_{opto} delay = 5 s) STDP (Fig. 1, L and M) resulted in only a slight enhancement. The actions of DA_{opto} were examined with various timings (Fig. 1N), revealing that DA_{opto} timing was critical to enhance plasticity, with maximal effects for a delay of 0.6 s (Fig. 1O and fig. S2, A to C), and decayed in a few seconds, which is consistent with behavioral study results (5, 16). The spine enlargement was accompanied by an increase in the 2pEPSC (fig. S3). A similar DA_{opto} timing was observed when we induced STDP through electrical stimulation of presynaptic fibers (fig. S4).

Pharmacological studies revealed that D1R-MSN structural plasticity was dependent on N-methyl-D-aspartate receptors (NMDARs), Ca^{2+}/calmodulin–dependent protein kinase II (CaMKII), and protein synthesis (Fig. 2A and fig. S5A), suggesting that the molecular mechanisms for D1R-MSN plasticity are similar to those underlying structural plasticity in hippocampal pyramidal neurons (10–12). Plasticity also depended on D1R and protein kinase A (PKA), but not on D2R (Fig. 2B and fig. S5A). Spine enlargement was prevented by an inhibitory peptide blocking the interaction of dopamine- and adenosine 3′,5′-cyclic monophosphate (cAMP)–regulated phosphoprotein 32 kD (DARPP-32) with protein phosphatase 1 (PP-1) (17), but not its control peptide (Fig. 2, C and D). Moreover, spine enlargement was induced even in the absence of DA_{opto} when PP-1 was inhibited by calyculin A (fig. S5, B and C). These results suggest that similar to hippocampal preparations (18), the phosphorylation of DARPP-32 by PKA would inhibit PP-1 and disinhibit CaMKII.

To test whether changes in Ca^{2+} signaling account for DA_{opto} timing (19), we imaged increases in cytosolic Ca^{2+} concentrations ($[Ca^{2+}]_i$) in spines using a low-affinity calcium indicator Fluo-4FF (K_{Ca} = 10 μM) to avoid saturation. The $[Ca^{2+}]_i$ increases gradually built up and quickly waned after cessation of the STDP protocol (Fig. 3A). We found that DA_{opto} did not affect Ca^{2+} transients (Fig. 3, B to D, and fig. S6, A to C), indicating that Ca^{2+} signaling modulation did not play a major role.

We examined whether CaMKII activation was related to DA_{opto} timing by using the Förster resonance energy transfer (FRET) indicator of CaMKII, Camuiα-CR (20–22), which was virally transfected into D1R-MSNs. CaMKII activation was weak in the absence of DA_{opto} (Fig. 3E) but was greatly potentiated by DA_{opto} (Fig. 3F), with timing similar to DA_{opto} timing for spine enlargement (Fig. 3G and fig. S6, D to F). This enhancement was specific to the stimulated spine (Fig. 3H), abolished by the inhibitory peptide for DARPP-32 (Fig. 3H and fig. S6G), and mimicked by PP-1 inhibitors, calyculin A and tautomycetin (fig. S6, H and I). These results support the hypothesis that PKA/DARPP-32 disinhibits CaMKII via PP-1 (fig. S11).

We addressed whether the DA_{opto} timing was formed at the level of PKA activation by using a FRET probe of PKA, AKAR2-CR (22), which was virally delivered to the D1R-MSNs. Unlike structural plasticity or Camuiα-CR activation, PKA activation in response to stimulation of a dendritic spine by STDP and DA_{opto} was not restricted to the stimulated spine; neighboring spines also exhibited significant PKA activation (fig. S7, A to D). Even without glutamate uncaging, PKA activation was observed in the spine and dendritic shaft (Fig. 4A) in an AP-dependent manner (Fig. 4B), suggesting that PKA activation is a cell-wide phenomenon. When DA_{opto} was applied at various times relative to APs, we obtained a timing (Fig. 4C and fig. S7, E to I) similar to DA_{opto} timing on spine enlargement and CaMKII activation (Fig. 1O). The extent of spine enlargement positively correlated with that of PKA activation (Fig. 4D). APs themselves were not sufficient to activate PKA (fig. S8, C to E). The contingency between APs and DA_{opto} might be detected by Ca^{2+}/calmodulin–dependent adenylyl cyclase 1 (AC1), which is synergistically activated by Ca^{2+}/calmodulin and Gs (23). Consistent with this, AC1 blocker (NB001) eliminated AKAR2 activation, as well as structural plasticity (fig. S9, A to D).

In the soma and proximal (first branch) dendrites, however, DA_{opto} alone was sufficient to activate PKA (Fig. 4E and fig S8, A and B) (24), and APs could only slightly enhance PKA. We predict that APs might have modulated spine enlargement to a small degree in these regions, if there had been spines (Fig. 4D). Thus, DA_{opto}-induced PKA activation must be suppressed in distal dendrites in order to attain the large dynamic range for the timing detection. In fact, when phosphodiesterase 10A (PDE10A), the major phosphodiesterase in MSNs, was blocked by its inhibitor papaverine (25), PKA activations were similarly induced in distal dendrites as in the soma (fig. S9, E to G). Papaverine also disrupted the time window for structural plasticity (fig. S9, H and I). Why were PDE10A actions particularly potent in the distal dendrites? Subcellular differences in PDE10A expression might not account for this, considering that PDE10A is expressed at the plasma membrane and is uniformly distributed along the dendrites (26). Instead, we found a negative correlation between dendrite diameter and DA_{opto}-induced PKA activity (fig. S10A, blue), which was lost when the phosphodiesterase was inhibited (fig. S10A, orange). Therefore, PDE10A might counteract the increases in cAMP more potently in the thin distal dendrites because of its high surface-to-volume ratios (fig. S10, B and C). Spines are only found in the distal thin dendrites of MSNs (fig. S10, D to E) (27), suggesting that spines are distributed to be efficiently modulated by dopamine timing in MSNs.

It has been enigmatic why dopamine reinforces preceding, but not subsequent, sensorimotor events. If dopamine always activates PKA, its effects should last long enough to reinforce the subsequent events over tens of seconds (Fig. 4A). However, dopamine did not activate PKA unless $[Ca^{2+}]_i$ primed AC1 to outcompete the high phosphodiesterase activity in thin dendrites (fig. S11). Our data show that $[Ca^{2+}]_i$ priming should occur strictly before dopamine delivery (0 s) (Figs. 1O, 3G, and 4C), which is reminiscent of serotonin's action in the classical conditioning of the siphon withdrawal reflex in *Aplysia* (28), in which serotonin, carrying an aversive signal, was only effective when it was preceded by increases in $[Ca^{2+}]_i$ for activation of calcium-dependent adenylyl cyclase (AC) and PKA in presynaptic terminals (29). The delay in $[Ca^{2+}]_i$ priming of AC may compensate the time lag of monoaminergic signals after reward or punishment. Our data suggest that reinforcement plasticity occurs at the single spine level, even though PKA activation is a cell-wide phenomenon, in such a way that dopamine regulates the gain of NMDAR-dependent Hebbian plasticity via CaMKII activity (fig. S11). This interdependence between Hebbian and reinforcement plasticity has been implicitly assumed in the reinforcement learning theory, in which the Hebbian term is used for the credit assignment (6, 30), and the dopamine timing in our study corresponds to the eligibility trace that determines the time window for reward action (30). Thus, we have clarified a molecular and cellular basis of reinforcement plasticity at the level of single dendritic spines.

REFERENCES AND NOTES

1. E. L. Thorndike, *Animal Intelligence* (Macmillan, New York, 1911).
2. I. P. Pavlov, *Conditioned Reflexes; An Investigation of the Physiological Activity of the Cerebral Cortex* (Oxford Univ. Press, Humphrey Milford, London, 1927).
3. M. F. Roitman, R. A. Wheeler, R. M. Carelli, *Neuron* **45**, 587–597 (2005).
4. Y. Dan, M. M. Poo, *Physiol. Rev.* **86**, 1033–1048 (2006).
5. J. Black, J. D. Belluzzi, L. Stein, *Brain Res.* **359**, 113–119 (1985).
6. W. Schultz, *J. Neurophysiol.* **80**, 1–27 (1998).
7. S. L. Smith-Roe, A. E. Kelley, *J. Neurosci.* **20**, 7737–7742 (2000).
8. T. Nakano, J. Yoshimoto, K. Doya, *Front. Comput. Neurosci.* **7**, 119 (2013).
9. M. Matsuzaki et al., *Nat. Neurosci.* **4**, 1086–1092 (2001).
10. M. Matsuzaki, N. Honkura, G. C. R. Ellis-Davies, H. Kasai, *Nature* **429**, 761–766 (2004).
11. J. Tanaka et al., *Science* **319**, 1683–1687 (2008).
12. C. D. Harvey, R. Yasuda, H. Zhong, K. Svoboda, *Science* **321**, 136–140 (2008).
13. C. R. Gerfen et al., *Science* **250**, 1429–1432 (1990).
14. W. Shen, M. Flajolet, P. Greengard, D. J. Surmeier, *Science* **321**, 848–851 (2008).
15. J. N. J. Reynolds, B. I. Hyland, J. R. Wickens, *Nature* **413**, 67–70 (2001).
16. R. A. Rescorla, *Annu. Rev. Neurosci.* **11**, 329–352 (1988).
17. Y. G. Kwon et al., *Proc. Natl. Acad. Sci. U.S.A.* **94**, 3536–3541 (1997).
18. R. D. Blitzer et al., *Science* **280**, 1940–1943 (1998).
19. C. Cepeda, M. S. Levine, *Sci. STKE* **2006**, pe20 (2006).
20. K. Takao et al., *J. Neurosci.* **25**, 3107–3112 (2005).
21. S. J. R. Lee, Y. Escobedo-Lozoya, E. M. Szatmari, R. Yasuda, *Nature* **458**, 299–304 (2009).
22. A. J. Lam et al., *Nat. Methods* **9**, 1005–1012 (2012).
23. G. D. Ferguson, D. R. Storm, *Physiology (Bethesda)* **19**, 271–276 (2004).
24. L. R. V. Castro et al., *J. Physiol.* **591**, 3197–3214 (2013).
25. A. Nishi et al., *J. Neurosci.* **28**, 10460–10471 (2008).
26. E. I. Charych, L. X. Jiang, F. Lo, K. Sullivan, N. J. Brandon, *J. Neurosci.* **30**, 9027–9037 (2010).
27. C. J. Wilson, P. M. Groves, *J. Comp. Neurol.* **194**, 599–615 (1980).
28. R. D. Hawkins, T. W. Abrams, T. J. Carew, E. R. Kandel, *Science* **219**, 400–405 (1983).
29. Y. Yovell, T. W. Abrams, *Proc. Natl. Acad. Sci. U.S.A.* **89**, 6526–6530 (1992).
30. R. S. Sutton, A. G. Barto, *Reinforcemnet Learning* (MIT Press, Cambridge, MA, 1998).

NITROGEN FIXATION

Ligand binding to the FeMo-cofactor: Structures of CO-bound and reactivated nitrogenase

Thomas Spatzal,[1]* Kathryn A. Perez,[1] Oliver Einsle,[2,3] James B. Howard,[1,4] Douglas C. Rees[1]*

The mechanism of nitrogenase remains enigmatic, with a major unresolved issue concerning how inhibitors and substrates bind to the active site. We report a crystal structure of carbon monoxide (CO)–inhibited nitrogenase molybdenum-iron (MoFe)–protein at 1.50 angstrom resolution, which reveals a CO molecule bridging Fe2 and Fe6 of the FeMo-cofactor. The μ_2 binding geometry is achieved by replacing a belt-sulfur atom (S2B) and highlights the generation of a reactive iron species uncovered by the displacement of sulfur. The CO inhibition is fully reversible as established by regain of enzyme activity and reappearance of S2B in the 1.43 angstrom resolution structure of the reactivated enzyme. The substantial and reversible reorganization of the FeMo-cofactor accompanying CO binding was unanticipated and provides insights into a catalytically competent state of nitrogenase.

Biological nitrogen fixation is nature's pathway to convert atmospheric dinitrogen (N_2) into a bioavailable form, ammonia (NH_3). Nitrogenase, the only known enzyme capable of performing this multielectron reduction, consists of two component metalloproteins, the iron (Fe)–protein (Av2) and the molybdenum-iron (MoFe)–protein (Av1) (1–3). The Fe-protein, containing a [4Fe:4S]-cluster, mediates the adenosine triphosphate (ATP)–dependent electron transfer to the MoFe-protein to support dinitrogen reduction (4). The MoFe-protein is an $\alpha_2\beta_2$ heterotetramer with one catalytic unit per $\alpha\beta$ heterodimer (5). To achieve the elaborate redox properties required for reducing the N–N triple bond, two metal centers are present in the MoFe-protein: the P-cluster and the FeMo-cofactor. The P-cluster, an [8Fe:7S] entity, is the initial acceptor for electrons, donated from the Fe-protein during complex formation between the two proteins (6–8). Electrons are subsequently transferred to the FeMo-cofactor, a [7Fe:9S:C:Mo]-R-homocitrate cluster that constitutes the active site for substrate reduction and is the most complex metal center known in biological systems (5, 9–12).

Substrates and inhibitors bind only to forms of the MoFe-protein reduced by two to four electrons relative to the resting, "as-isolated" state, which can only be generated in the presence of reduced Fe-protein and ATP (1). Mechanistic studies must take into account the dynamic nature of the nitrogenase system, which requires multiple association and dissociation events between the two component proteins, as well as the ubiquitous presence of protons that are reduced to dihydrogen even in competition with other substrates (1, 13–15). The resulting distribution of intermediates under turnover conditions complicates the structural and spectroscopic investigation of substrate interactions. Hence, even the fundamental question of whether molybdenum or iron represents the site for substrate binding at the FeMo-cofactor is still under debate, and as a consequence, a variety of mechanistic pathways have been proposed based on either molybdenum or iron as the catalytic center, mainly following Chatt-type chemistry (16).

Inhibitors are potentially powerful tools for the preparation of stably trapped transient states that could provide insight into the multielectron reduction mechanism. In this regard, carbon monoxide (CO), a noncompetitive inhibitor for all substrates except protons (17, 18), has a number of attractive properties; CO is isoelectronic to the physiological substrate, is a reversible inhibitor, and only binds to partially reduced MoFe-protein generated under turnover condi-

tions. Although noncompetitive inhibitors are traditionally considered to bind at distinct sites from the substrate, for complex enzymes—such as nitrogenase—with multiple oxidation states and potential substrate-binding modes, this distinction is not required (19). More recently, it has also been shown that CO is a substrate, albeit a very poor one, whose reduction includes concomitant C–C bond formation to generate C2 and longer-chain hydrocarbons, in a reaction reminiscent of the Fischer-Tropsch synthesis (20, 21). Therefore, CO binding as inhibitor or substrate must involve important active-site properties common to the reduction of the natural substrate dinitrogen. For this reason, CO binding has been investigated by a variety of spectroscopic methods, most notably electron paramagnetic resonance and infrared spectroscopy, and depending on the partial pressure, multiple CO-bound species have been observed; yet, a structurally explicit description of any CO-binding site has been elusive (18, 22–27).

Building on these observations, we have determined a high-resolution crystal structure of a CO-bound state of the MoFe-protein from *Azotobacter vinelandii*. This necessitated overcoming several obstacles. First, the experimental setup for all protein-handling steps, including crystallization, was deemed to require the continuous presence of CO. Second, because inhibition requires enzyme turnover, a prerequisite was the ability to obtain crystals of the MoFe-protein from activity assay mixtures, rather than from isolated protein (see supplementary material for assay details), conditions that are typically contradictory to crystallization requirements. Finally, rapid MoFe-protein crystallization (≤5 hours) was crucial and was achieved on the basis of previously developed protocols in combination with seeding strategies and in the presence of CO (10).

Crystals of the inhibited MoFe-protein (Av1-CO) yielded structural data at 1.50 Å resolution, which allowed clear identification of a CO ligand (Fig. 1, A and C, and fig. S1, A to D). The Av1-CO structure directly demonstrates the binding of one molecule of CO per active site in a μ_2-bridging mode between Fe2 and Fe6 that forms one edge of the trigonal six-iron prism (Fe2-3-4-5-6-7) of the FeMo-cofactor (Fig. 1, A, C, and D). CO binding is accompanied by a displacement of one of the belt sulfur atoms (S2B), although it retains the essentially tetrahedral coordination spheres for Fe2 and Fe6. As a result, the two Fe are coordinated by two sulfur and two carbon atoms—a geometry, to our knowledge, not previously observed in metalloclusters [although higher–coordination number geometries have

[1]Howard Hughes Medical Institute and Division of Chemistry and Chemical Engineering, MailCode 114-96, California Institute of Technology, Pasadena, CA 91125, USA. [2]Institut für Biochemie, Albert-Ludwigs-Universität Freiburg, 79104 Freiburg, Germany. [3]BIOSS Centre for Biological Signalling Studies, Albert-Ludwigs-Universität Freiburg, 79104 Freiburg, Germany. [4]Department of Biochemistry, Molecular Biology and Biophysics, University of Minnesota, Minneapolis, MN 55455, USA.
*Corresponding author. E-mail: spatzal@caltech.edu (T.S.); dcrees@caltech.edu (D.C.R.)